SCIENTIFIC REPORTS

OPEN

Magnetism of coupled spin tetrahedra in ilinskite-type $KCu_5O_2(SeO_3)_2Cl_3$

Received: 13 October 2017
Accepted: 15 January 2018
Published online: 05 February 2018

Danis I. Badrtdinov[1], Elena S. Kuznetsova[2], Valeriy Yu. Verchenko[2,3], Peter S. Berdonosov[2], Valeriy A. Dolgikh[2], Vladimir V. Mazurenko[1] & Alexander A. Tsirlin[1,4]

Synthesis, thermodynamic properties, and microscopic magnetic model of ilinskite-type $KCu_5O_2(SeO_3)_2Cl_3$ built by corner-sharing Cu_4 tetrahedra are reported, and relevant magnetostructural correlations are discussed. Quasi-one-dimensional magnetic behavior with the short-range order around 50 K is rationalized in terms of weakly coupled spin ladders (tubes) having a complex topology formed upon fragmentation of the tetrahedral network. This fragmentation is rooted in the non-trivial effect of the SeO_3 groups that render the Cu–O–Cu superexchange strongly ferromagnetic even at bridging angles exceeding 110°.

In frustrated magnets, competing spin-spin interactions give rise to unusual types of magnetic order having potential implications for magnetoelectric materials[1] and complex magnetic textures, such as skyrmions[2,3]. An even more exotic behavior is realized for magnetic ions with spins-$\frac{1}{2}$ supporting strong quantum fluctuations that keep spins dynamic down to zero temperature and may give rise to novel phases of quantum spin liquids[4,5]. Extensive theoretical research on frustrated spin systems faces a shortage of model compounds that would allow experimental probe of the intricate magnetic phenomena anticipated by theory.

Natural minerals boast highly diverse crystal structures, where different spatial arrangements of the magnetic ions mimic frustrated spin lattices. For example, Cu-based minerals have been instrumental in recent research on the spin-$\frac{1}{2}$ kagome problem of the two-dimensional (2D) spin lattice of corner-sharing triangles, an enigmatic magnetic model that evades rigorous analytical solution and causes vivid debate regarding the nature of its ground state[6,7]. Many other frustrated spin lattices, ranging from simple[8] or less than simple[9] spin chains to exotic maple-leaf varieties of the depleted triangular lattice[10], can be realized in the minerals too.

Cu_4 tetrahedra centered by oxygen atoms are a typical building block of copper mineral crystal structures[11]. Such tetrahedra can also be viewed as a simple frustrated unit, because they comprise four spin triangles. Here, we report synthesis and magnetic behavior of $KCu_5O_2(SeO_3)_2Cl_3$, a sibling of the mineral ilinskite[12,13], where Cu_4 tetrahedra form layers in the *bc* plane (Fig. 6a). Disregarding the tetrahedral picture, the layers can also be viewed as zigzag (sawtooth) chains running along the *b* direction and bridged by sparse Cu linkers. Given persistent interest in theoretical studies of the sawtooth (delta) chains[14–17] and low-dimensional frameworks of spin tetrahedra[18–23], as well as the dearth of relevant model materials, we chose to explore magnetic behavior of $KCu_5O_2(SeO_3)_2Cl_3$ and elucidate its interaction topology. To this end, we combine experimental probes with extensive first-principles calculations, because magnetic interactions in Cu-based minerals are far from trivial[24–27]. $KCu_5O_2(SeO_3)_2Cl_3$ is no exception indeed.

Results

Synthesis and crystal structure. Ilinskite is a rare mineral. Its natural samples are too small for most of the experimental probes, whereas previous synthetic attempts reported preparation of only tiny single crystals obtained in a mixture with other copper selenite chlorides[28]. Therefore, we developed a synthesis method to produce ilinskite-type compounds in larger quantities. Polycrystalline samples of $KCu_5O_2(SeO_3)_2Cl_3$ were synthesized from

[1]Theoretical Physics and Applied Mathematics Department, Ural Federal University, 620002, Ekaterinburg, Russia. [2]Department of Chemistry, Moscow State University, 119991, Moscow, Russia. [3]National Institute of Chemical Physics and Biophysics, 12618, Tallinn, Estonia. [4]Experimental Physics VI, Center for Electronic Correlations and Magnetism, Institute of Physics, University of Augsburg, 86135, Augsburg, Germany. Correspondence and requests for materials should be addressed to D.I.B. (email: reason2205@yandex.ru) or A.A.T. (email: altsirlin@gmail.com)

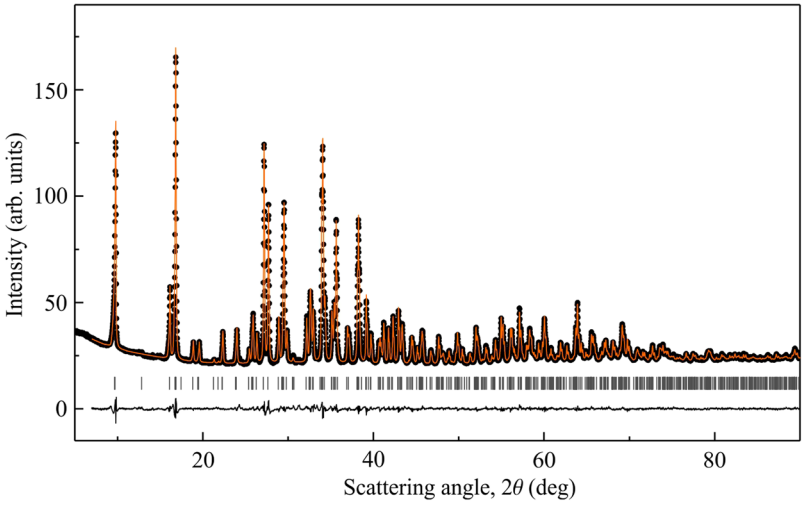

Figure 1. Rietveld refinement of the powder XRD data for the $KCu_5O_2(SeO_3)_2Cl_3$ sample used in this work. Ticks show peak positions according to the lattice parameters given in the text. The refinement residuals are $R_I = 0.019$, $R_p = 0.013$, and $R_{wp} = 0.018$.

binary oxide and chloride precursors in sealed quartz tubes at 380–400 °C (see Methods for details). X-ray diffraction (XRD) data for such samples are consistent with the crystal structure reported previously[28], Fig. 1.

An extensive description of the ilinskite-type structures has been given in refs[13,28]. Here, we focus only on those aspects that are germane to the magnetic behavior. In Cu^{2+} compounds, the relevant coordination environment is typically a plaquette formed by four shortest Cu-ligand contacts that define the plane of the magnetic ($d_{x^2-y^2}$) orbital, where x and y are local directions within the plaquette.

Four crystallographic positions of Cu split into two groups. Cu1 and Cu4 form CuO_4-type plaquettes with 4 Cu–O distances of about 1.9–2.0 Å, whereas a distant contact to the Cl atom at 2.59 Å (Cu1) and 2.92 Å (Cu4) plays no role in the magnetic exchange[29–31], because orbitals of the Cl atom do not overlap with the magnetic orbital of Cu^{2+}. In the case of Cu2 and Cu3, the plaquettes are of $CuClO_3$ type, which is also not uncommon in Cu-based magnets[32,33]. Here, the Cu–O distances are in the same 1.9–2.0 Å range, whereas the Cu–Cl distance is 2.19 Å (Cu2) and 2.37 Å (Cu3), and p-orbitals of the Cl atoms hybridize with the magnetic $d_{x^2-y^2}$ orbital of Cu^{2+}.

Viewing the crystal structure of $KCu_5O_2(SeO_3)_2Cl_3$ from the Cu plaquettes perspective, we find well-defined layers in the bc plane (Fig. 2a). The layers are bridged by SeO_3 groups and additionally interleaved by the K^+ ions. Each layer can be seen as a sequence of -Cu1-Cu4-Cu2-Cu4-Cu1- zigzag chains along the b direction, with sparse links along the c direction via Cu3. With magnetic interactions restricted to nearest neighbors (Cu–O–Cu bridges), one expects the magnetic topology of spin planes formed by corner-sharing Cu_4 tetrahedra (Fig. 6). However, Cl atoms are known to mediate long-range superexchange interactions, which render the spin lattice a lot more complex[32,34,35]. Our microscopic analysis reported below identifies additional long-range interactions indeed. Even more importantly, dissimilar interactions within the tetrahedra largely relieve the frustration compared to the regular tetrahedral geometry.

Thermodynamic properties. Magnetic susceptibility of $KCu_5O_2(SeO_3)_2Cl_3$ shows a broad maximum around 50 K and a weak upturn below 8 K (Fig. 3). The suppression of this upturn in higher magnetic fields indicates its impurity origin. At high temperatures, the susceptibility obeys the Curie-Weiss law $\chi(T) = \frac{C}{T-\Theta}$ with the Curie constant $C = 2.3$ emu K/mol and Curie-Weiss temperature $\theta = -60$ K. The negative value of θ implies antiferromagnetic (AFM) nature of leading exchange interactions. The C value yields an effective moment of 1.91 μ_B/Cu, slightly larger than the spin-only moment of 1.73 μ_B for Cu^{2+}. This leads to an effective g-value of $g = 2.2$.

The susceptibility maximum around $T_{\max} \simeq 50$ K indicates AFM short-range order. In low-dimensional spin systems, signatures of a magnetic transition are often blurred, because the transition occurs below T_{max}, and the ordered moment is only a fraction of the total magnetic moment[36,37]. Nevertheless, in many of the Cu^{2+} compounds the transitions, even if they occur well below $T_{\max}$, are clearly visible as kinks in $\chi(T)$[29] or as the divergence of the low-field and high-field susceptibilities[38,39]. This is not the case in $KCu_5O_2(SeO_3)_2Cl_3$, though. Heat-capacity data likewise show no obvious transition anomalies down to 1.8 K in good agreement with the magnetic susceptibility (Fig. 4, right). Further analysis of the specific heat is complicated by the fact that no suitable non-magnetic reference exists for ilisnkite-type compounds, so that lattice and magnetic contributions to the specific heat can not be separated at this point.

At the first glance, the susceptibility curve for $KCu_5O_2(SeO_3)_2Cl_3$ may be reminiscent of a $S = 1/2$ uniform Heisenberg chain (UHC) with the nearest-neighbor antiferromagentic exchange interaction J. In such a chain, the position and amplitude of the susceptibility maximum yield $\chi^{\rm chain}_{\max}(T_{\max})T_{\max}g^{-2} = 0.0353229(3)$ emu K/mol[40]. This parameter is independent of J, thus providing a simple test whether the UHC model might be applicable. In our case, $\chi_{\max}$ at $T_{\max} \simeq 50$ K is 0.0175 emu/mol. Using $g = 2.2$, we obtain 0.0362 emu K/mol(per Cu) in reasona-

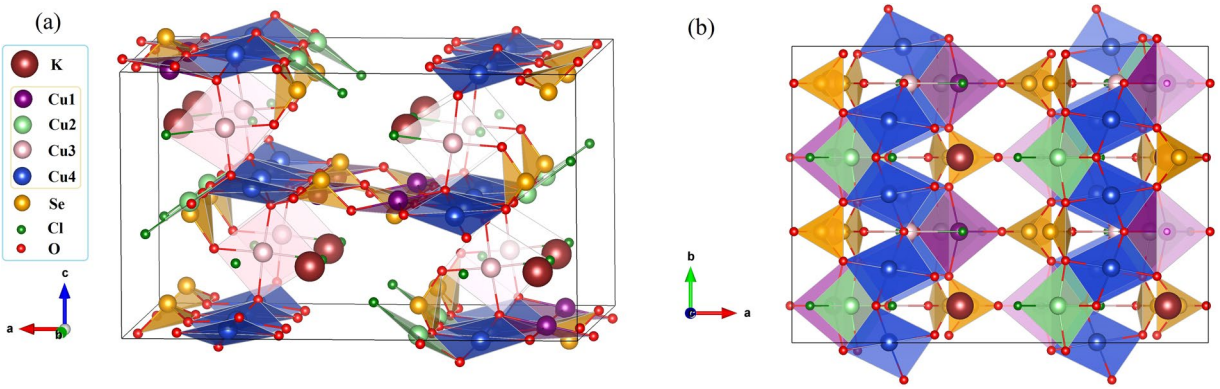

Figure 2. (**a**,**b**) Crystal structure of $KCu_5O_2(SeO_3)_2Cl_3$ in the *ac* and *ab* projections. Crystal structures are visualized by using the VESTA software[61].

ble agreement with the UHC model. However, we show below that the magnetic model of $KCu_5O_2(SeO_3)_2Cl_3$ is much more involved, and similarities with the susceptibility of the UHC are purely accidental.

Although the susceptibility decreases upon cooling below 50 K, it does not decay exponentially, as would be expected in a gapped spin system. Magnetization isotherm measured at 1.5 K reveals a finite slope of $M(H)$ at low fields, which also excludes the presence of a spin gap. The $M(H)$ curve changes slope around 15 T and shows the increasing trend up to at least 50 T, the highest field reached in our experiment.

Magnetic model. For the microscopic description of the magnetic properties of $KCu_5O_2(SeO_3)_2Cl_3$, we construct a minimal Heisenberg-type Hamiltonian that takes into account all the leading exchange interactions between magnetic moments. To this end, we use density functional theory (DFT) methods.

The structural complexity of $KCu_5O_2(SeO_3)_2Cl_3$ (Fig. 2) is reflected in its intricate electronic spectrum. Indeed, the calculated DFT band structure at the Fermi level obtained with a minimal unit cell is characterized by numerous dispersive and strongly overlapping bands. This band structure is metallic, because it is calculated on the GGA level without taking Coulomb correlations into account. Despite the complexity, one can easily determine the particular copper states producing the bands at the Fermi level. The valence of Cu ions in $KCu_5O_2(SeO_3)_2Cl_3$ is equal to 2+, placing one unpaired electron to the $d_{x^2-y^2}$ orbital that forms bands in the vicinity of the Fermi level.

We use this fact for constructing the minimal tight-binding model in the Wannier function basis, which gives preliminary information concerning magnetic interactions in the system in question. Figure 5 shows a comparison between the full DFT spectrum and the spectrum of the tight-binding Hamiltonian. The tight-binding model reproduces the DFT solution very accurately. The corresponding hopping integrals between Wannier functions are presented in Table 1. Here, we neglect long-range hopping parameters with amplitudes $|t| \leq 50$ meV.

Six leading nonequivalent hoppings (t_1, t_2, t_6, t_7, t_8 and t_{11}) are close to 150 meV. Five of the underlying superexchange pathways are between nearest neighbors. On the other hand, t_{11} is a long-range interaction between the Cu atoms separated by 6.448 Å. This clearly identifies the importance of interactions beyond nearest neighbors in $KCu_5O_2(SeO_3)_2Cl_3$. Although AFM contributions to the exchange can be directly expressed as $J_i^{\mathrm{AFM}} = 4t_i^2/U_{\mathrm{eff}}$, with the effective on-site Coulomb repulsion U_{eff}, ferromagnetic (FM) contributions are usually non-negligible. Therefore, we restrict ourselves to the 11 potentially relevant interactions listed in Table 1 (all nearest-neighbor couplings and three leading long-range couplings), and directly proceed to calculating total exchange couplings $J = J^{\mathrm{AFM}} + J^{\mathrm{FM}}$ using the DFT + U method, where Coulomb correlations are taken into account on the mean-field level. DFT + U restored the anticipated insulating solution with the energy gap of 4.4 eV and magnetic moment of 0.75 μ_B on copper atoms.

The full set of the isotropic exchange couplings in $KCu_5O_2(SeO_3)_2Cl_3$ was calculated by a mapping procedure for total energies[41,42]. These results are presented in Table 1. The change in the U parameter of DFT + U (on-site Coulomb repulsion) leads to a systematic reduction in the magnitudes of J's, because both AFM and FM contributions are reduced when electronic localization is enhanced. The reduction in the AFM part of the exchange is due to the $1/U$ dependence of J^{AFM}. The reduction in J^{FM} can be ascribed to the fact that FM superexchange in cuprates depends on the hybridization of the Cu $d_{x^2-y^2}$ orbital with ligand orbitals[43], an effect suppressed by the enhanced electron localization at higher U's.

Magnetostructural correlations. The calculated nearest-neighbor exchange couplings can be divided into AFM (1–2, 6–8) and FM (3–5) groups. Simple magnetostructural correlations rooted in Goodenough-Kanamori-Anderson rules suggest FM superexchange for Cu–O–Cu angles close to 90° and AFM superexchange away from 90°. This argument explains the $J_2 > J_1$ trend, but fails to address peculiarities of other nearest-neighbor couplings that typically feature larger angles but weaker AFM (J_7, J_8) or even FM (J_4, J_5) exchanges compared to J_2. One natural reason for this difference is the presence of two bridging oxygen atoms for J_1 and J_2 vs. a single oxygen bridge for $J_3 - J_8$. However, this does not explain the drastic difference between the strongly AFM J_6 with the angle of 112° and sizable FM J_4 and J_5 with the even higher angles of 114° and 113°, respectively.

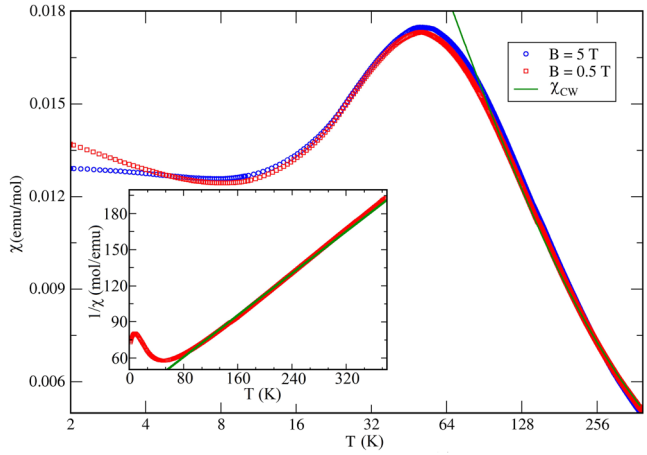

Figure 3. Magnetic susceptibility $\chi(T)$ for $KCu_5O_2(SeO_3)_2Cl_3$ obtained under different values of the external magnetic field in the field-cooling regime. The inset shows the Curie-Weiss approximation in the 100–380 K temperature range with the parameters $\theta = 60$ K and C = 2.3 emu K/mol, as denoted by the green line.

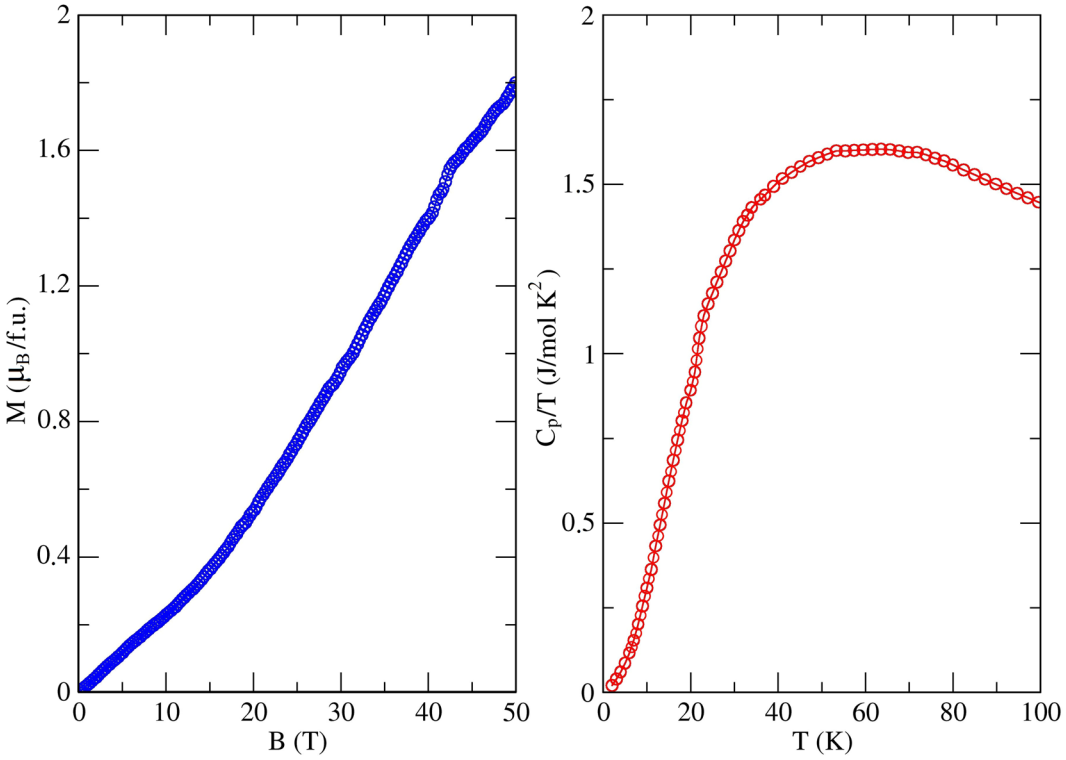

Figure 4. (Left panel) The magnetization curve measured at $T = 1.5$ K. (Right panel) Temperature dependence of the specific heat, $C_p(T)/T$, for $KCu_5O_2(SeO_3)_2Cl_3$ measured in zero field.

The twisting of the copper-oxygen plaquettes is another structural parameter relevant to the superexchange[24]. For example, the superexchange between the orthogonal CuO_4 plaquettes can remain FM even if the Cu–O–Cu angle departs from 90° reaching 100–105°[44]. One may suggest that this trend persists at higher bridging angles, as observed in $KCu_5O_2(SeO_3)_2Cl_3$. However, this twisting argument does not seem to explain peculiarities of our case, because diheral angles between the Cu^{2+} plaquettes for the ferromagnetic couplings J_4 (122°) and J_5 (119°) are larger than that for the antiferromagnetic coupling J_6 (90°). Therefore, the FM couplings occur between less twisted plaquettes, whereas the AFM coupling takes place between the more twisted plaquettes, and, in contrast to ref.[44], the twisting does not enhance ferromagnetism. We thus conclude that side groups should be at play here. Indeed, a closer examination of the crystal structure shows that the FM couplings J_4 and J_5 are associated with SeO_3 links between the copper plaquettes. The coupling J_6 lacks such a link and is, therefore, AFM. Likewise, the AFM nature of J_7 should be traced back not only to its larger Cu–O–Cu angle compared to that of $J_3 - J_6$, but also to the absence of the SeO_3 link.

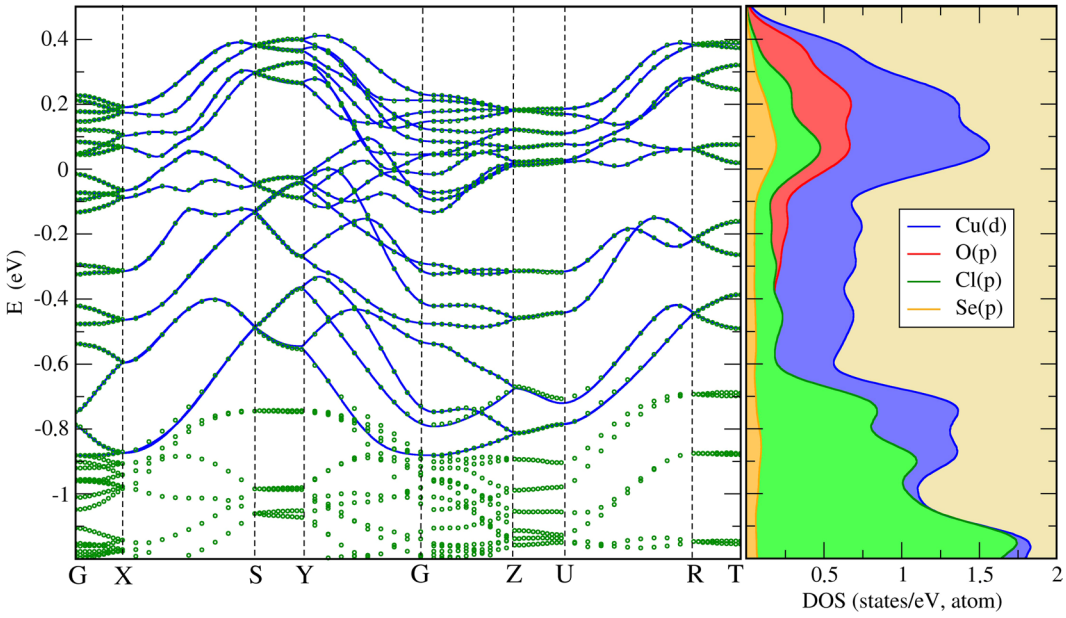

Figure 5. (Left panel) Band structure of $KCu_5O_2(SeO_3)_2Cl_3$ near the Fermi level calculated on the GGA level. The green dotted lines denote the results of the GGA calculation, whereas the blue lines correspond to a minimal tight-binding model constructed in the Wannier function basis. (Right panel) Corresponding atomic-resolved densities of states (DOS).

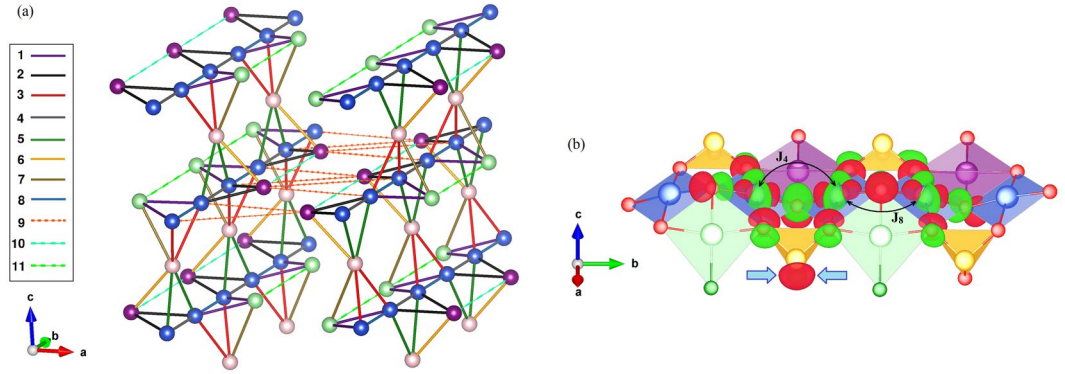

Figure 6. (**a**) Schematic representation of magnetic interactions between the copper atoms in the $KCu_5O_2(SeO_3)_2Cl_3$ structure. (**b**) Wannier functions centered on copper atoms within the structural chain. The blue arrows indicate the sizable overlap of the Wannier functions at the Se sites, the effect that underlies the large difference between J_4 and J_8. Different colors denote different phases of the Wannier functions.

The effect of the SeO_3 groups can be visualized by comparing the interactions J_4 and J_8 (Fig. 6b), where for the sake of clarity we choose J_8 instead of J_6. The Wannier functions of the copper atoms interacting via J_4 have a significant overlap on Se. In contrast, the Wannier functions for J_8 do not show such an overlap, and this interaction is restricted to the conventional Cu–O–Cu link. The additional overlap channel, which is a joint effect of selenium and next-nearest oxygen states, may produce the ferromagnetic contribution and eventually lead to the ferromagnetic sign of J_4[27].

Lastly, we discuss the long-range couplings J_9 - J_{11}. All of them are mediated by the SeO_3 groups, as typical for polyanionic compounds, where non-magnetic anions provide shorter O–O distances that are favorable for the Cu–O…O–Cu superexchange. Generally, the nature of the long-range couplings is kinetic. They are strongly dependent on the orbital overlap and, therefore, on the linearity of the Cu–O…O–Cu superexchange pathway quantified by the Cu–O–O angle(s). When such a path deviates from linear, the coupling is suppressed[45,46]. In the case of J_{11}, the Cu–O–O angle is equal to 170°. For J_{10} and J_9, the corresponding angles are smaller, 163° and 157°, respectively. This trend fully captures the hierarchy of the long-range exchange couplings in $KCu_5O_2(SeO_3)_2Cl_3$.

Comparison to the experiment. Within the high-temperature expansion of the magnetic susceptibility, the Curie-Weiss temperature θ can be expressed through the sum of the exchange couplings J_{ij} in the following form (for the Cu atom i):

	$Cu(i) - Cu(j)$	d_{Cu-Cu}	angle	t_{ij}	J_{ij} $U_d = 8$ eV	J_{ij} $U_d = 9$ eV	J_{ij} $U_d = 10$ eV	J_{ij}^{QMC}
1	Cu2−Cu4	2.854	90,95	138.57	3.24	1.86	0.88	—
2	Cu1−Cu4	2.946	101, 93	158.58	14.33	10.70	7.73	6.38
3	Cu3−Cu4	3.148	113	−110.39	−0.45	−1.13	−1.49	—
4	Cu4−Cu4	3.168	114	−30.49	−9.52	−7.91	−6.29	−7.91
5	Cu3−Cu4	3.173	113	−52.33	−10.95	−9.31	−7.68	−5.60
6	Cu1−Cu3	3.174	112	162.72	17.55	9.88	7.30	5.95
7	Cu2−Cu3	3.277	116	160.81	13.38	10.50	8.07	6.29
8	Cu4−Cu4	3.280	121	−144.72	10.44	7.52	5.31	7.52
9	Cu1−Cu4	6.250	—	−81.37	4.64	3.56	2.67	—
10	Cu1−Cu1	6.448	—	−96.79	9.48	7.62	5.98	7.62
11	Cu2−Cu2	6.448	—	−139.15	17.64	14.35	11.36	14.35

Table 1. Magnetic interactions in $KCu_5O_2(SeO_3)_2Cl_3$: crystallographic positions of the interacting copper atoms, the Cu–Cu distances d (in Å), the relevant Cu–O–Cu bridging angles (in deg), hopping parameters t_{ij} (in meV), and total exchange couplings J_{ij} (in K) obtained from DFT + U. The last column represents optimized values used in QMC simulations. The negative signs of the exchange integrals stand for ferromagnetic interactions. See Fig. 6 for details of the interaction network.

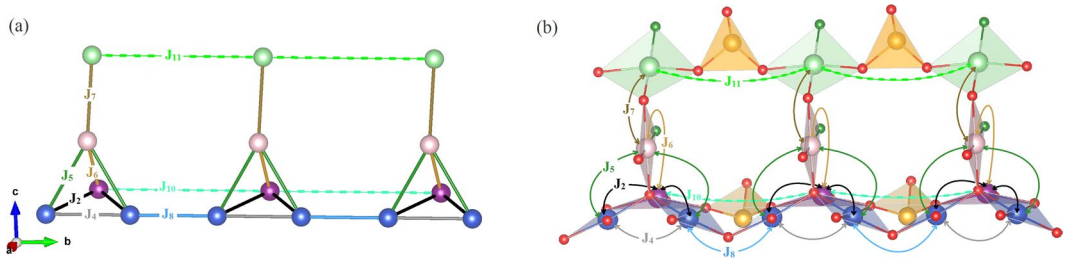

Figure 7. (**a**) Magnetic model used in the QMC simulations. (**b**) Exchange interactions within the crystal structure.

$$\theta_i = -\frac{S(S+1)}{3k_B}\sum_j J_{ij}, \tag{1}$$

where the summation runs over all pairs of copper atom connected by J_{ij}, k_B is Boltzmann constant, and $S = \frac{1}{2}$. Having averaged the Curie-Weiss temperatures calculated for nonequivalent Cu sites within the unit cell, we obtain $\theta = -91$ K, -60 K, and -38 K for $U = 8$ eV, 9 eV, and 10 eV, respectively. Comparing the theoretical estimates to the experimental value of $\theta = -60$ K, we find best agreement for the set of J's calculated with $U = 9$ eV.

The spin lattice of $KCu_5O_2(SeO_3)_2Cl_3$ is frustrated due to the triangles formed by the AFM interactions $J_1 - J_1 - J_8$ and $J_8 - J_9 - J_9$. The triangles with two FM couplings J_3 and one AFM coupling J_8 further contribute to the frustration. This prevents us from simulating magnetic properties of the full three-dimensional DFT-based spin model. However, frustrating interactions are relatively weak compared to the others. Therefore, the non-frustrated model can be introduced as a reasonable approximation when the weaker couplings J_1, J_3, and J_9 are neglected. This decouples the layers of the tetrahedra, because they are connected via J_9 only, and further splits the layers into chains with a complex topology (Fig. 7). A spin-ladder (tube) motif with J_2, J_5, J_6, and J_7 acting as legs, and J_4, J_8, J_{10}, and J_{11} acting as rungs, can be recognized. The overall geometry is very exotic, though, and clearly lacks any counterpart in theoretical studies of low-dimensional spin systems. Because individual tubes lack magnetic frustration, they are amenable to QMC simulations.

QMC simulations of the magnetic susceptibility reproduce the position of the maximum, but not its amplitude (Fig. 8, left). By varying exchange parameters, we found that the agreement with the experiment can be largely improved if the rung couplings are renormalized by a factor of 0.6. The resulting exchange parameters used in the QMC fit are listed in the last column of Table 1. The renormalization can be related to the frustrated nature of $KCu_5O_2(SeO_3)_2Cl_3$. Removing the frustration requires the reduction in at least part of the remaining couplings.

We also used the exchange couplings from the last column of Table 1 to simulate the magnetization curve (Fig. 8, right). In agreement with the experiment, we find a steady increase in $M(H)$ up to 50 T. At higher fields, the curve bends and eventually reaches saturation around 250 T, the field beyond the reach of present-day pulsed magnets. The 15 T bend is not reproduced in our simulation. It may be due to anisotropic terms in the spin Hamiltonian, which are beyond the scope of our consideration. It is also worth noting that the simulated curve shows no plateau at zero magnetization, and the gapless nature of the system is well reproduced microscopically. The non-trivial shape of the magnetization curve is likely related to the step-wise saturation of different spins in the lattice. The first bend at

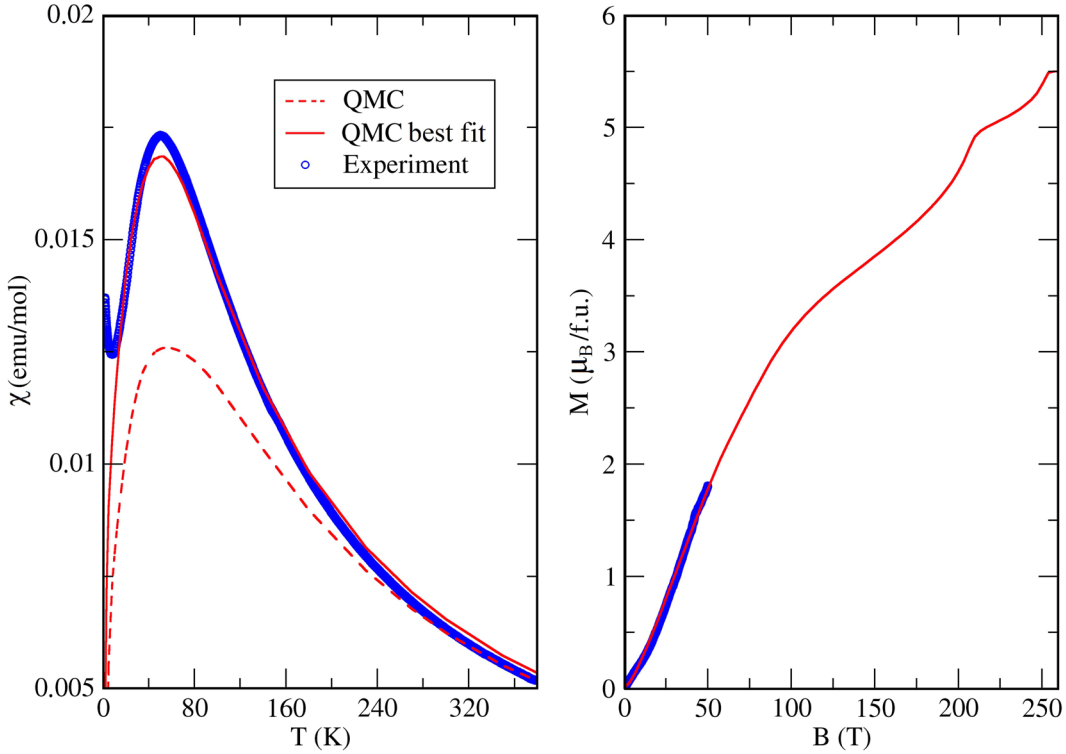

Figure 8. Comparison with the experiment. (Left panel) Magnetic susceptibility obtained within QMC at 0.5 T. The straight line corresponds to the QMC results for the exchange parameters from the last column of Table 1, whereas the dashed line is for the parameters obtained from DFT without further adjustment. (Right panel) The magnetization curve from QMC simulations with optimized exchange parameters (last column of Table 1). Experimental data are shown with empty circles.

∼110 T and around $\frac{3}{5}$ of the total magnetization is due to the polarization of the three spins connected via ferromagnetic J_4 and J_5 (Fig. 7). The second bend near ∼210 T may be related to the polarization of the fourth spin in the tetrahedron (suppression of the AFM J_2 and J_6). Finally, all spins are polarized around 250 T.

Discussion and Summary

The spin lattice of $KCu_5O_2(SeO_3)_2Cl_3$ features layers of corner-sharing Cu_4 tetrahedra. This relatively simple geometrical motif is amended by the long-range couplings J_{10} and J_{11}, but a more drastic effect stems from the different nature of the bonds on the edges of each tetrahedron. Both FM and AFM exchanges occur between nearest neighbors, and the frustration is largely relieved. Microscopically, this effect originates from a combination of the Cu–O–Cu superexchange pathways and SeO_3 bridges that, albeit non-magnetic and seemingly benign, alter Wannier orbitals of Cu^{2+} and affect not only the size but also the sign of the exchange coupling. An equally unanticipated influence of the non-magnetic side groups on the superexchange has been recently reported in the mineral szeniscite[27], where MoO_4 bridges have an effect opposite to the SeO_3 case. They largely enhance the AFM couplings at the bridging angles of about 105°, which are nearly 10° smaller than the bridging angles for $J_3 - J_7$ in $KCu_5O_2(SeO_3)_2Cl_3$.

Extending this analysis to other Cu-based magnets, we realize that the SeO_3 groups are often responsible for FM contributions to the exchange. For example, J^{FM} of −120 K was reported in $CuSe_2O_5$[47], whereas FM interactions between nearest neighbors in francisite, $Cu_3Bi(SeO_3)_2O_2Cl$[31,48,49], may also be influenced by the SeO_3 links. The Cu–O–Cu angles of the fracisite structure are, in fact, in the same range of 110–115°, where, according to our results, both FM and AFM interactions may occur depending on the presence or absence of the SeO_3 link. The SeO_3 groups can thus have an indirect, but strong influence on the superexchange, rendering Cu^{2+} selenites an interesting if somewhat unpredictable class of quantum magnets.

$KCu_5O_2(SeO_3)_2Cl_3$ reveals clear signatures of low-dimensional magnetic behavior. Short-range AFM order is formed around 50 K. This behavior can be rationalized on the microscopic level by the spin lattice comprising robust non-frustrated one-dimensional (1D) units with only weak and frustrated couplings between them. Néel temperatures of quasi-1D spin-$\frac{1}{2}$ antiferromagnets are sometimes orders of magnitude lower than leading exchange couplings along the 1D units[47,50]. Inconspicuous signatures of the long-range order in such systems may be hard to detect. Therefore, local probes, such as nuclear magnetic resonance (NMR) or muon spin relaxation (μSR), will be instrumental in revealing the possible long-range order of $KCu_5O_2(SeO_3)_2Cl_3$ at low temperatures. This work goes beyond the scope of our present study.

In summary, we prepared single-phase polycrystalline samples of ilinskite-type $KCu_5O_2(SeO_3)_2Cl_3$ and studied its magnetic behavior. Short-range AFM order sets in below 50 K, whereas no clear signatures of long-range

magnetic ordering are seen down to 2 K, and no spin gap is observed. This behavior is rationalized microscopically in terms of non-frustrated 1D spin ladders (tubes) with relatively weak and frustrated couplings between the 1D units. The crystal structure of $KCu_5O_2(SeO_3)_2Cl_3$ features layers of corner-sharing Cu_4 tetrahedra. Most of the exchange couplings take place between nearest neighbors, but dissimilar interactions on the edges of these tetrahedra largely reduce the frustration and render the spin lattice quasi-1D. This non-trivial effect originates from an inconspicuous influence of the non-magnetic SeO_3 groups that alter superexchange and also mediate long-range couplings.

Methods

Polycrystalline samples of $KCu_5O_2(SeO_3)_2Cl_3$ were synthesized using the ampoule technique with KCl, CuO, $CuCl_2$, and SeO_2 as reactants. KCl was dried at 140 °C prior to synthesis. SeO_2 was prepared by the dehydration of selenous acid under vacuum (0.05–0.08 Torr) and purified by sublimation in the flow of dry air and NO_2. Stoichiometric amounts of the reactants were mixed in an Ar-filled glove box. About 1 g of the mixture was loaded into an evacuated and sealed quartz tube and annealed under the following protocol: (i) heating to 300 °C for 12 hours; (ii) annealing at 300 °C for 24 hours; (iii) heating to the synthesis temperature T_{syn} for 12 hours; (iv) annealing at T_{syn} for 7 days. T_{syn} was varied between 350 and 500 °C and had tangible effect on the sample color that varied from emerald green at lower T_{syn} to dark-brown at higher T_{syn}. Single-phase samples of $KCu_5O_2(SeO_3)_2Cl_3$ were obtained at $T_{syn} = 380$–400 °C and had green color.

Sample quality was checked by x-ray diffraction (XRD) using the STOE STADI-P ($CuK_{\alpha 1}$ radiation, transmission mode) and PanAlytical X'PERT III (CuK_α radiation, reflection mode) lab diffractometers. Rietveld refinement of the XRD data using the Jana2006[51] program yields lattice parameters of $KCu_5O_2(SeO_3)_2Cl_3$, $a = 18.133(8)$ Å, $b = 6.438(3)$ Å, and $c = 10.546(6)$ Å. All peaks could be assigned to the ilinskite-type structure (Fig. 1).

Magnetic susceptibility of $KCu_5O_2(SeO_3)_2Cl_3$ was measured on a powder sample using the vibrating sample magnetometer (VSM) option of the Physical Properties Measurement System (PPMS) from Quantum Design. The data were collected in the temperature range 2–380 K under external magnetic fields of 0–14 T in the field-cooling regime. Magnetization isotherm up to 50 T was measured at 1.5 K in pulsed magnetic fields at the Dresden High Magnetic Field Laboratory. A description of the experimental setup can be found elsewhere[52]. The pulsed-field data were scaled using the PPMS data collected up to 14 T.

Magnetic exchange couplings were obtained from first-principles calculations within the framework of density functional theory (DFT) with the generalized gradient approximation (GGA) for the exchange-correlation potential[53]. To this end, the Quantum Espresso[54] and VASP[55,56] packages were utilized. The energy cutoff in the plane-wave decomposition was set to 400 eV, and the energy convergence criteria was chosen at 10^{-8} eV. For the Brillouin-zone integration a $5 \times 5 \times 5$ Monkhorst-Pack mesh was used. The minimal model was constructed in the basis of maximally localized Wannier functions (MLWF)[57], where Cu $d_{x^2-y^2}$ states were used as initial projectors.

Exchange parameters J_{ij} of the Heisenberg model

$$\hat{\mathcal{H}} = \sum_{i<j} J_{ij} \hat{\mathbf{S}}_i \hat{\mathbf{S}}_j \tag{2}$$

with $S = \frac{1}{2}$ and the summation over bonds $\langle ij \rangle$, were calculated by a mapping procedure[41]. Strong correlation effects were accounted for on the mean-field GGA + U level[58] with the on-site Hund's exchange $J_H = 1$ eV and the on-site Coulomb repulsion U varied from 8 to 10 eV.

Quantum Monte Carlo simulations were performed using the stochastic series expansion (SSE)[59] method implemented in the ALPS simulation package[60]. Simulations were performed on a finite lattice of $N = 1000$ spins $S = \frac{1}{2}$ with periodic boundary conditions.

References

1. Cheong, S.-W. & Mostovoy, M. Multiferroics: a magnetic twist for ferroelectricity. *Nature Materials* **6**, 13–20 (2007).
2. Okubo, T., Chung, S. & Kawamura, H. Multiple-*q* states and the skyrmion lattice of the triangular-lattice heisenberg antiferromagnet under magnetic fields. *Phys. Rev. Lett.* **108**, 017206 (2012).
3. Leonov, A. O. & Mostovoy, M. Multiply periodic states and isolated skyrmions in an anisotropic frustrated magnet. *Nature Comm.* **6**, 8275 (2015).
4. Balents, L. Spin liquids in frustrated magnets. *Nature* **464**, 199–208 (2010).
5. Savary, L. & Balents, L. Quantum spin liquids: a review. *Rep. Prog. Phys.* **80**, 016502 (2017).
6. Mendels, P. & Bert, F. Quantum kagome frustrated antiferromagnets: One route to quantum spin liquids. *C. R. Phys.* **17**, 455–470 (2016).
7. Norman, M. R. Colloquium: Herbertsmithite and the search for the quantum spin liquid. *Rev. Mod. Phys.* **88**, 041002 (2016).
8. Caslin, K. *et al.* Characterization of the spin-(1)/(2) linear-chain ferromagnet $CuAs_2O_4$. *Phys. Rev. B* **89**, 014412 (2014).
9. Jeschke, H. *et al.* Multistep approach to microscopic models for frustrated quantum magnets: The case of the natural mineral azurite. *Phys. Rev. Lett.* **106**, 217201 (2011).
10. Fennell, T., Piatek, J., Stephenson, R. A., Nilsen, G. & Rønnow, H. Spangolite: an $s = 1/2$ maple leaf lattice antiferromagnet? *J. Phys.: Condens. Matter* **23**, 164201 (2011).
11. Krivovichev, S., Mentré, O., Siidra, O., Colmont, M. & Filatov, S. Anion-centered tetrahedra in inorganic compounds. *Chem. Rev.* **113**, 6459–6535 (2013).
12. Vergasova, L., Semenova, T., Shuvalov, R., Filatov, S. & Ananiev, V. Ilinskite $NaCu_5O_2(SeO_3)_2Cl_3$–a new mineral of volcanic exhalations. *Dokl. Akad. Nauk* **353**, 641–644 (1997).
13. Krivovichev, S., Filatov, S. & Vergasova, L. The crystal structure of ilinskite, $NaCu_5O_2(SeO_3)_2Cl_3$, and review of mixed-ligand CuO_mCl_n coordination geometries in minerals and inorganic compounds. *Miner. Petrol.* **107**, 235–242 (2013).
14. Sen, D., Shastry, B. S., Walstedt, R. E. & Cava, R. Quantum solitons in the sawtooth lattice. *Phys. Rev. B* **53**, 6401–6405 (1996).
15. Nakamura, T. & Kubo, K. Elementary excitations in the δ chain. *Phys. Rev. B* **53**, 6393–6400 (1996).

16. Krivnov, V. Y., Dmitriev, D. V., Nishimoto, S., Drechsler, S.-L. & Richter, J. Delta chain with ferromagnetic and antiferromagnetic interactions at the critical point. *Phys. Rev. B* **90**, 014441 (2014).
17. Dmitriev, D. V. & Krivnov, V. Y. Delta chain with anisotropic ferromagnetic and antiferromagnetic interactions. *Phys. Rev. B* **92**, 184422 (2015).
18. Starykh, O. A., Singh, R. R. P. & Levine, G. C. Spinons in a crossed-chains model of a 2D spin liquid. *Phys. Rev. Lett.* **88**, 167203 (2002).
19. Sindzingre, P., Fouet, J.-B. & Lhuillier, C. One-dimensional behavior and sliding Luttinger liquid phase in a frustrated spin-1/2 crossed chain model: Contribution of exact diagonalizations. *Phys. Rev. B* **66**, 174424 (2002).
20. Brenig, W. & Grzeschik, M. Valence-bond crystal phase of the crossed-chain quantum spin model. *Phys. Rev. B* **69**, 064420 (2004).
21. Starykh, O. A., Furusaki, A. & Balents, L. Anisotropic pyrochlores and the global phase diagram of the checkerboard antiferromagnet. *Phys. Rev. B* **72**, 094416 (2005).
22. Bishop, R. F., Li, P. H. Y., Farnell, D. J. J., Richter, J. & Campbell, C. E. Frustrated Heisenberg antiferromagnet on the checkerboard lattice: $J_1 - J_2$ model. *Phys. Rev. B* **85**, 205122 (2012).
23. Li, P. H. Y. & Bishop, R. F. Ground-state phase structure of the spin-(1)/(2) anisotropic planar pyrochlore. *J. Phys.: Condens. Matter* **27**, 386002 (2015).
24. Lebernegg, S., Tsirlin, A. A., Janson, O. & Rosner, H. Two energy scales of spin dimers in clinoclase $Cu_3(AsO_4)(OH)_3$. *Phys. Rev. B* **87**, 235117 (2013).
25. Lebernegg, S., Tsirlin, A. A., Janson, O., Redhammer, G. J. & Rosner, H. Interplay of magnetic sublattices in langite $Cu_4(OH)_6SO_4 \cdot 2H_2O$. *New J. Phys.* **18**, 033020 (2016).
26. Janson, O. *et al.* Magnetic behavior of volborthite $Cu_3V_2O_7(OH)_2 \cdot 2H_2O$ determined by coupled trimers rather than frustrated chains. *Phys. Rev. Lett.* **117**, 037206 (2016).
27. Lebernegg, S. *et al.* Frustrated spin chain physics near the Majumdar-Ghosh point in szenicsite $Cu_3(MoO_4)(OH)_4$. *Phys. Rev. B* **95**, 035145 (2017).
28. Kovrugin, V. M., Siidra, O. I., Colmont, M., Mentré, O. & Krivovichev, S. V. Emulating exhalative chemistry: synthesis and structural characterization of ilinskite, $Na[Cu_5O_2](SeO_3)_2Cl_3$, and its K-analogue. *Mineralogy and Petrology* **109**, 421–430 (2015).
29. Tsirlin, A. A., Janson, O., Lebernegg, S. & Rosner, H. Square-lattice magnetism of diaboleite $Pb_2Cu(OH)_4Cl_2$. *Phys. Rev. B* **87**, 064404 (2013).
30. Jeschke, H. O., Salvat-Pujol, F. & Valent, R. First-principles determination of Heisenberg Hamiltonian parameters for the spin-(1)/(2) kagome antiferromagnet $ZnCu_3(OH)_6Cl_2$. *Phys. Rev. B* **88**, 075106 (2013).
31. Rousochatzakis, I., Richter, J., Zinke, R. & Tsirlin, A. A. Frustration and Dzyaloshinsky-Moriya anisotropy in the kagome francisites $Cu_3Bi(SeO_3)_2O_2X$ (X = Br, Cl). *Phys. Rev. B* **91**, 024416 (2015).
32. Valent, R., Saha-Dasgupta, T., Gros, C. & Rosner, H. Halogen-mediated exchange in the coupled-tetrahedra quantum spin systems $Cu_2Te_2O_5X_2$ (X = Br,Cl). *Phys. Rev. B* **67**, 245110 (2003).
33. Berdonosov, P. S. *et al.* Crystal structures and variable magnetism of $PbCu_2(XO_3)_2Cl_2$ with X = Se, Te. *Dalton Trans.* **42**, 9547 (2013).
34. Tsirlin, A. A. & Rosner, H. Structural distortion and frustrated magnetic interactions in the layered copper oxychloride (CuCl) $LaNb_2O_7$. *Phys. Rev. B* **79**, 214416 (2009).
35. Tsirlin, A. A. & Rosner, H. Microscopic model of (CuCl)$LaNb_2O_7$: Coupled spin dimers replace a frustrated square lattice. *Phys. Rev. B* **82**(R), 060409 (2010).
36. Lancaster, T. *et al.* Magnetic order in the $S = 1/2$ two-dimensional molecular antiferromagnet copper pyrazine perchlorate $Cu(Pz)_2(ClO_4)_2$. *Phys. Rev. B* **75**, 094421 (2007).
37. Tsirlin, A. A. *et al.* Hidden magnetic order in CuNCN. *Phys. Rev. B* **85**, 224431 (2012).
38. Woodward, F. M., Albrecht, A. S., Wynn, C. M., Landee, C. P. & Turnbull, M. M. Two-dimensional $S = 1/2$ Heisenberg antiferromagnets: Synthesis, structure, and magnetic properties. *Phys. Rev. B* **65**, 144412 (2002).
39. Janson, O. *et al.* Long-range superexchange in $Cu_2A_2O_7$ (A = P, As, V) as a key element of the microscopic magnetic model. *Phys. Rev. B* **83**, 094435 (2011).
40. Johnston, D. C. *et al.* Thermodynamics of spin $S = 1/2$ antiferromagnetic uniform and alternating-exchange heisenberg chains. *Phys. Rev. B* **61**, 9558 (2000).
41. Xiang, H., Lee, C., Koo, H.-J., Gong, X. & Whangbo, M.-H. Magnetic properties and energy-mapping analysis. *Dalton Trans.* 823–853 (2013).
42. Tsirlin, A. A. Spin-chain magnetism and uniform Dzyaloshinsky-Moriya anisotropy in BaV_3O_8. *Phys. Rev. B* **89**, 014405 (2014).
43. Mazurenko, V. V., Skornyakov, S. L., Kozhevnikov, A. V., Mila, F. & Anisimov, V. I. Wannier functions and exchange integrals: The example of $LiCu_2O_2$. *Phys. Rev. B* **75**, 224408 (2007).
44. Nath, R. *et al.* Magnetization and spin dynamics of the spin $S = 1/2$ hourglass nanomagnet $Cu_5(OH)_2(NIPA)_4 \cdot 10H_2O$. *Phys. Rev. B* **87**, 214417 (2013).
45. Janson, O. *et al.* $CaCu_2(SeO_3)_2Cl_2$: Spin-(1)/(2) Heisenberg chain compound with complex frustrated interchain couplings. *Phys. Rev. B* **83**, 144423 (2011).
46. Nath, R. *et al.* Hindered magnetic order from mixed dimensionalities in CuP_2O_6. *Phys. Rev. B* **89**, 014407, https://doi.org/10.1103/PhysRevB.89.014407 (2014).
47. Janson, O. *et al.* Electronic structure and magnetic properties of the spin-1/2 Heisenberg system $CuSe_2O_5$. *New J. Phys.* **11**, 113034 (2009).
48. Prishchenko, D. A. *et al.* Antiferroelectric instability in the kagome francisites $Cu_3Bi(SeO_3)_2O_2X$ (X = Cl, Br). *Phys. Rev. B* **95**, 064102 (2017).
49. Constable, E. *et al.* Magnetic and dielectric order in the kagomelike francisite $Cu_3Bi(SeO_3)_2O_2Cl$. *Phys. Rev. B* **96**, 014413 (2017).
50. Lancaster, T. *et al.* Persistent dynamics in the $S = 1/2$ quasi-one-dimensional chain compound $Rb_4Cu(MoO_4)_3$ probed with muon-spin relaxation. *Phys. Rev. B* **85**, 184404 (2012).
51. Petříček, V., Dušek, M. & Palatinus, L. Crystallographic computing system JANA2006: General features. *Z. Krist.* **229**, 345–352 (2014).
52. Tsirlin, A. A. *et al.* Exploring the spin-(1)/(2) frustrated square lattice model with high-field magnetization studies. *Phys. Rev. B* **80**, 132407 (2009).
53. Perdew, J. P., Burke, K. & Ernzerhof, M. Generalized gradient approximation made simple. *Phys. Rev. Lett.* **77**, 3865–3868 (1996).
54. Giannozzi, P. *et al.* QUANTUM ESPRESSO: a modular and open-source software project for quantum simulations of materials. *J. Phys.: Condens. Matter* **21**, 395502 (2009).
55. Kresse, G. & Furthmüller, J. Efficiency of ab-initio total energy calculations for metals and semiconductors using a plane-wave basis set. *Computa. Mater. Sci.* **6**, 15 (1996).
56. Kresse, G. & Furthmüller, J. Efficient iterative schemes for *ab initio* total-energy calculations using a plane-wave basis set. *Phys. Rev. B* **54**, 11169–11186 (1996).
57. Marzari, N. & Vanderbilt, D. Maximally localized generalized Wannier functions for composite energy bands. *Phys. Rev. B* **56**, 12847–12865 (1997).
58. Anisimov, V. I., Zaanen, J. & Andersen, O. K. Band theory and Mott insulators: Hubbard *U* instead of Stoner. *I. Phys. Rev. B* **44**, 943–954 (1991).
59. Sandvik, A. W. & Kurkijärvi, J. Quantum Monte Carlo simulation method for spin systems. *Phys. Rev. B* **43**, 5950 (1991).

60. Albuquerque, A. *et al*. The ALPS project release 1.3: Open-source software for strongly correlated systems. *J. Magn. Magn. Mater.* **310**, 1187 (2007).
61. Momma, K. & Izumi, F. *VESTA* 3 for three-dimensional visualization of crystal, volumetric and morphology data. *J. Appl. Crystallogr.* **44**, 1272–1276 (2011).

Acknowledgements

The work of D.I.B. and V.V.M. was supported by the grant of the President of Russian Federation No. MD-6458.2016.2. The work in Tallinn was supported by the European Regional Development Fund, project TK134. A.A.T. acknowledges financial support by the Federal Ministry for Education and Research through the Sofja Kovalevskaya Award of Alexander von Humboldt Foundation. We acknowledge the support of the HLD at HZDR, member of EMFL, and thank Yurii Skourski for the pulsed-field magnetization measurement on $KCu_5O_2(SeO_3)_2Cl_3$.

Author Contributions

E.S.K., P.S.B., and V.A.D. synthesized and characterized the samples, V.Y.V. performed magnetization and specific heat measurements, D.I.B. performed numerical simulations and, together with V.V.M. and A.A.T., wrote the manuscript. P.S.B. proposed the idea, A.A.T. supervised the project. All the authors contributed to the analysis and interpretation of the results.

Additional Information

Competing Interests: The authors declare that they have no competing interests.

Publisher's note: Springer Nature remains neutral with regard to jurisdictional claims in published maps and institutional affiliations.